

Learning Contact Dynamics through Touching: Action-conditional Graph Neural Networks for Robotic Peg Insertion

Zongyao Yi*, Joachim Hertzberg^{†*} and Martin Atzmueller^{†*}

Abstract—We present a learnable physics-based predictive model that provides accurate motion and force-torque prediction of the robot end effector in contact-rich manipulation. The proposed model extends the state-of-the-art GNN-based simulator (FIGNet) with novel node and edge types, enabling action-conditional predictions for control and state estimation in the context of robotic peg insertion. Our model learns in a self-supervised manner, using only joint encoder and force-torque data while the robot is touching the environment. In simulation, the MPC agent using our model matches the performance of the same controller with the ground truth dynamics model in a challenging peg-in-hole task, while in the real-world experiment, our model achieves a 50% improvement in motion prediction accuracy and 3× increase in force-torque prediction precision over the baseline physics simulator. Finally, we apply the model to track the robot end effector with a particle filter during real-world peg insertion, demonstrating a practical application of its predictive accuracy. Source code and supplementary materials are available on the project’s website: <https://sites.google.com/view/act-fignet>.

I. INTRODUCTION

Precise assembly tasks like peg insertion require robots to operate under constant contact with rigid and unyielding environment, such as a fixed electrical socket. Unlike interaction with movable objects, these environments are non-compliant and pose hard geometric constraints on the robot’s motion. This makes action-conditional prediction of motion and forces non-trivial, as violating these constraints can cause excessive contact forces and potentially damage the robot. Analytical physics simulators [1], [2] struggle with modeling such complex contact dynamics in the real world because the point-contact assumptions commonly used in these simulators start to break down when surface contacts dominate. Recent work has shown that Graph Neural Networks (GNNs) are more capable of approximating real-world contact dynamics [3], [4]. However, most existing GNN-based approaches focus on current state to next state prediction; the effects of control inputs are not explicitly modeled. Moreover, these methods cannot directly predict contact forces and require privileged training data, e.g., fully observed trajectories of free falling objects, which is hard to obtain in the real-world. In this paper, we extend a state-of-the-art GNN simulator (FIGNet) [4] with action-conditional graph layers to predict the robot end effector’s motion and force-torque feedback given current state and action. Our model requires only robot joint encoder and force-torque

sensor data for training in a self-supervised manner, while still inherits the precise contact resolution from FIGNet. The resulting model not only learns the smooth dynamics of the robot end effector in the absence of contacts, but also the discontinuities when contacts engage. In simulation, we deploy the learned model with model-predictive control on a challenging peg insertion task and achieve a high success rate comparable to that of the ground-truth simulator. In the real-world experiment, our model outperforms the fine-tuned MuJoCo baseline in terms of prediction accuracy. In summary, this paper makes the following contributions:

- Integrate action-conditional graph layers with the state-of-the-art GNN-based forward model [4], and provide a learnable dynamics and observation model tailored for peg-in-hole tasks;
- showcase the effectiveness of the learned model in model-based control with peg insertion tasks in simulation;
- demonstrate the model’s prediction accuracy with real-world data and its potential usage for state estimation in combination with a particle filter.

II. RELATED WORK

A. GNN-based physics simulators

Pioneering work on learning dynamics for control purposes using graph-structured representations includes [5], [6]. While [5] uses graph neural (GN) blocks to model interacting neighbor entities, PropNet [6] introduces propagation networks to facilitate long-range interactions. Both systems achieve superior performance on model-based control, and demonstrate strong generalization ability to unseen scenes and tasks. However, these approaches focus on the interactions between simple dynamic particles/links, contacts resulting from more complex geometries are not considered. Hence, their use-cases are limited to simple scenarios, e.g., swinging pendulum [5] and box pushing [6]. To model more delicate contact behaviors, [3], [4], [7] utilize mesh-based representations and encode the interactions between mesh vertices and faces using a deeper GNN architecture. More recently, [8] further extends the mesh representation with higher-order topology and embeds physics laws into the GNN message-passing layers. While achieving state-of-the-art prediction accuracy, their approaches focus on free-falling rigid bodies, and the learned dynamics model is not action-conditioned, restricting their use in control and inference tasks. In contrast to the previous work, our approach inherits the state-of-the-art accuracy from [4], while modeling the

*German Research Center for Artificial Intelligence, DFKI Niedersachsen, Osnabrück, Germany zongyao.yi@dfki.de

[†]Osnabrück University, Institute of Computer Science, Osnabrück, Germany

action-conditional behaviors of the robot during contact-rich manipulation tasks at the same time.

B. Contact force prediction

A precise contact force prediction model is essential in contact-rich manipulation. For example, it can help to avoid hazardous actions of the robot that generate large contact forces, and provide a discriminative observation model when using probabilistic filters such as particle filters for state estimation [9]–[12]. However, work on learnable action-conditional force prediction is relatively scarce. [9] uses a binary force observation model, but relies on a predefined force threshold and is conditioned on the contact state only. A notable approach in this area is presented in [13], where a linear model is fitted to predict the F/T readings from the feature vector, i.e. concatenation of the robot’s configuration and applied control. But since the environment structure is implicitly encoded, it may not generalize well to unseen scenarios, for example, with unprecedented connector/socket geometries. On the other hand, our model can learn the underlying contact mechanism by encoding geometries and actions in separate graph structures, and shows strong generalization ability to unseen environments and out-of-distribution actions. [12] uses particle filters coupled with an analytical rigid-body simulator to jointly estimate contact forces, object poses, and geometries. But this approach assumes that the rigid bodies are always in force equilibrium state. In contrast, our approach makes no such assumptions and can learn both smooth dynamics and discontinuous contact behaviors.

III. METHOD

A. Problem statement

A manipulation task can be modeled as a discrete-time partially observable Markov decision process (POMDP) with a state space \mathcal{S} , an action space \mathcal{A} , an observation space \mathcal{O} , transition dynamics $\mathcal{T} : \mathcal{S} \times \mathcal{A} \rightarrow \mathcal{S}$, and observation model $\Omega : \mathcal{S} \times \mathcal{A} \rightarrow \mathcal{O}$. Here, we consider the state, action, and observation space to be continuous, i.e., $\mathcal{S} \subseteq \mathbb{R}^{d_s}$, $\mathcal{A} \subseteq \mathbb{R}^{d_a}$, and $\mathcal{O} \subseteq \mathbb{R}^{d_o}$. The goal of the proposed model is to (1) approximate the transition dynamics \mathcal{T} with a prediction function $g : \mathcal{S} \times \mathcal{A} \rightarrow \mathcal{S}$, such that the prediction error $\|g(s_t, a_t) - s_{t+1}\|_2$ is minimized; and (2) approximate the observation model Ω with a function $h : \mathcal{S} \times \mathcal{A} \rightarrow \mathcal{O}$, minimizing the observation error $\|h(s_t, a_t) - o_t\|_2$.

B. Setup

In this work, we focus on the peg-in-hole task, where the interaction between the hand-mounted tool and the environment is of particular interest. We assume that the robot operates under Cartesian space controllers, e.g., impedance or force controllers. This allows us to simplify the robot structure to a system consisting only of the tool body and the environment (i.e., the peg and the hole, see Fig. 5e), with the floating tool body moving in response to the applied force and torque, thereby making the system robot-independent.

The system configuration is represented in maximal coordinates, where the tool body is fully described by its position, orientation, linear and angular velocity in a global reference frame. The tool body has 6 DoF and is not subjected to any constraints other than those imposed by contacts. The system state can then be written as $s_t = [\mathbf{x}_t, \dot{\mathbf{x}}_t]$, where $\mathbf{x}_t \in \mathbb{R}^7$ is the 3-D position and 4-D quaternion, and $\dot{\mathbf{x}}_t \in \mathbb{R}^6$ is the linear and angular velocities. The control input to the system is the 6-D external wrench acting directly on the tool body: $a_t = [\mathbf{f}_t, \boldsymbol{\tau}_t] \in \mathbb{R}^6$, where \mathbf{f}_t and $\boldsymbol{\tau}_t$ are the 3-D force and torque respectively. To implicitly estimate and make use of higher-order quantities, e.g., acceleration, the prediction model takes as input a sequence of previous states $[s_t, \dots, s_{t-h+1}]$, shorthand as \mathbf{s}_t^h . Together with the current action a_t , the model is designed to predict the next state \hat{s}_{t+1} and the reaction force-torque from the tool body, i.e., the F/T sensor reading, which is defined as the sole observation of the system, denoted as $\hat{o}_t = [\hat{\mathbf{f}}_t, \hat{\boldsymbol{\tau}}_t]$.

a) Geometry representation: The tool body and the environment geometries are represented with triangle meshes. Each mesh consists of a set of vertices $\{\mathbf{p}^{m_i}\}$, with $\mathbf{p}^{m_i} \in \mathbb{R}^3$; and a set of faces indicating the connections among vertices, which are triplets of vertex indices: $\{\mathcal{F}_k\}$, with $\mathcal{F}_k = (m_{k_1}, m_{k_2}, m_{k_3})$.

b) Graph representation: A directed graph is defined as an ordered pair of nodes and edges $\mathcal{G} = (\mathcal{V}, \mathcal{E})$. \mathcal{V} is an ordered set of nodes $\{v_i\}$, with $v_i \in \mathbb{R}^{d_v}$ the node feature vector of dimension d_v ; and \mathcal{E} is a set of node index pairs $\{(i, j)\}$ and the corresponding edge feature vectors $\{e_{i \rightarrow j}\}$, with $e_{i \rightarrow j} \in \mathbb{R}^{d_e}$ and d_e the edge feature dimension.

C. Pipeline

The pipeline consists of three main components: a graph constructor, the encoder-processor-decoder (EPD) stack, and the post-processing module. Most parts of the implementation follow the recipe of [4] with two key extensions: (1) we extend the model to explicitly take action as part of the inputs, by introducing action-conditional node and edge types; (2) the model can predict the reaction force-torque by decoding the newly introduced edge features. The pipeline first prepares the input graph from \mathbf{s}_t^h and a_t given other static system information, including the object meshes¹ and their static attributes, i.e., mass, friction coefficient. This graph construction process can be written as $\mathcal{G}^{\text{in}} = \Phi_{\text{con}}(\mathbf{s}_t^h, a_t, \mathcal{M})$, where \mathcal{G}^{in} is the input graph, and system information is denoted as \mathcal{M} . Subsequently, the encoder-processor-decoder stack is applied to the input graph, written as $\mathcal{G}^{\text{out}} = \Psi_{\theta}(\mathcal{G}^{\text{in}})$, where θ is the learnable parameters of the stack. Finally, the post-processing module reads out \mathcal{G}^{out} to obtain the prediction state \hat{s}_{t+1} and observation \hat{o}_t , which in our case is the force-torque feedback from the tool body. This final process can be written as $\hat{s}_{t+1}, \hat{o}_t = \Phi_{\text{post}}(\mathcal{G}^{\text{out}}, \mathcal{M})$. This pipeline aims at approximating the aforementioned transition and observation functions g and h combined. Fig. 1

¹Note that each object can have multiple meshes, as most collision detection libraries require convex meshes. It is common practice to decompose complex meshes into several simpler convex components.

gives an overview of the pipeline. In the following, each component is described in detail.

1) *Graph construction*: As the first step, the system dynamics is encoded in a heterogeneous graph consisting of three types of nodes, namely mesh nodes \mathcal{V}^M , object nodes \mathcal{V}^O and the newly introduced virtual world nodes \mathcal{V}^W . Mesh nodes encode mesh vertices and their features are the concatenation of the vertex velocities and per-object static attributes, i.e., mass, friction coefficient, and a binary variable indicating whether the object is dynamic. Object nodes are calculated likewise, but with the object center-of-mass (CoM) positions instead. Bidirectional object-mesh edges $\mathcal{E}^{O \leftrightarrow M}$ are created between object nodes and the mesh nodes belonging to the same objects; their features are the relative displacements between the object CoM and the mesh vertices. Intra-object mesh-mesh edges $\mathcal{E}^{M \leftrightarrow M}$ connect mesh nodes of the colliding mesh faces, whose features encode contact information and are calculated according to [4] (see Appendix V-A.2.b). Fig. 2 visualizes the graph construction process.

As one of the key extensions of [4] to handle the influence of control inputs, we introduce the virtual world nodes and the world-mesh edges $\mathcal{E}^{W \leftrightarrow M}$. Per-object virtual world node pairs, i.e., type-force \mathbf{v}_f^W and type-torque \mathbf{v}_τ^W , are connected to their corresponding mesh nodes in both directions to account for the different effects of force and torque. For example, in our system with only the tool and environment bodies, a pair of world nodes is assigned to each of them. This can be readily extended to multi-robot setups, simply by appending additional pairs of world nodes. The world node features are one-hot vectors differentiating their types (force/torque), while the world-mesh edge features are the direction and magnitude of the applied force/torque. For static bodies, the edge features are simply zero vectors (more in Appendix V-A.2.a). To summarize, the resulting input graph is defined as $\mathcal{G}^{\text{in}} = (\mathcal{V}^M, \mathcal{V}^O, \mathcal{V}^W, \mathcal{E}^{M \leftrightarrow M}, \mathcal{E}^{O \leftrightarrow M}, \mathcal{E}^{W \leftrightarrow M})$. In the following, we use $\mathbf{v}^{X,l}$ and $\mathbf{e}_{X \rightarrow Y}^l$ to denote node and edge features, where $X, Y \in \{M, O, W\}$ are placeholders for different node types, and the superscript $(\cdot)^l$ indicates the message passing layer.

2) *Encoder-Processor-Decoder*: First, the encoders map the node and edge features to latent embeddings:

$$\mathbf{v}_i^{X,1} = \phi_{\mathcal{V}^X}^{\text{enc}}(\mathbf{v}_i^{X,\text{feature}}) \quad (1)$$

$$\mathbf{e}_{X_s \rightarrow Y_r}^1 = \phi_{\mathcal{E}^{X \rightarrow Y}}^{\text{enc}}(\mathbf{e}_{X_s \rightarrow Y_r}^{\text{feature}}) \quad (2)$$

The processor consists of N message-passing layers, and each layer performs edge feature updates followed by message aggregation and node feature updates:

$$\mathbf{e}_{X_s \rightarrow Y_r}^{l+1} = \phi_{\mathcal{E}^{X \rightarrow Y}}^{\text{proc}_l}([\mathbf{e}_{X_s \rightarrow Y_r}^l, \mathbf{v}_s^{X,l}, \mathbf{v}_r^{Y,l}]) \quad (3)$$

$$\mathbf{v}_r^{Y,l+1} = \phi_{\mathcal{V}^Y}^{\text{proc}_l}([\mathbf{v}_r^{Y,l}, \sum_s \mathbf{e}_{X_s \rightarrow Y_r}^{l+1}]) \quad (4)$$

Finally, the latent node/edge embeddings in the final graph are passed to the decoders. Mesh node embeddings are decoded into the accelerations of the individual mesh vertices:

$$\hat{\mathbf{a}}_i^{m_i} = \phi_{\mathcal{V}^M}^{\text{dec}}(\mathbf{v}_i^{M,N}) \quad (5)$$

As the second extension to [4], the reaction force and torque is calculated by decoding the world-mesh edges pointing from the tool mesh nodes to the world nodes:

$$\hat{\mathbf{f}}_t = \frac{1}{\mathcal{N}_{\text{tool}}} \sum_{i=1}^{\mathcal{N}_{\text{tool}}} \phi_{\mathcal{E}^{M \rightarrow W}}^{\text{dec}}(\mathbf{e}_{m_i \rightarrow f}^N) \quad (6)$$

$$\hat{\mathbf{\tau}}_t = \frac{1}{\mathcal{N}_{\text{tool}}} \sum_{i=1}^{\mathcal{N}_{\text{tool}}} \phi_{\mathcal{E}^{M \rightarrow W}}^{\text{dec}}(\mathbf{e}_{m_i \rightarrow \tau}^N) \quad (7)$$

with $\mathcal{N}_{\text{tool}}$ the number of mesh vertices in the tool body. The functions in this module ($\phi^{\text{enc}}, \phi^{\text{proc}}, \phi^{\text{dec}}$) are all implemented as 2-layer MLPs (see Appendix V-B for details).

3) *Post-processing*: First, the predicted vertex positions are calculated by an Euler integration of the predicted accelerations with two previous vertex positions: $\hat{\mathbf{p}}_{t+1}^{m_i} = \hat{\mathbf{a}}_t^{m_i} + 2\mathbf{p}_t^{m_i} - \mathbf{p}_{t-1}^{m_i}$. Subsequently, the next body pose can be calculated by matching the predicted and untransformed mesh vertices: $\hat{\mathbf{x}}_{t+1} = \mathcal{T}^{-1}(\hat{\mathbf{p}}_{t+1}^{m_i}, \mathbf{p}_{\text{ref}}^{m_i})$, where \mathcal{T}^{-1} denotes the point alignment process, and the implementation is provided by PyTorch3D [14]. Finally, the predicted velocity is calculated as $\hat{\mathbf{x}}_{t+1} = (\hat{\mathbf{x}}_{t+1} - \mathbf{x}_t)/dt$.

D. Training

a) *Dataset*: The EPD stack is trained with the dataset of the form $\{(\mathbf{s}_k^h, a_k, o_k, s_{k+1})_{k=1 \dots D}\}$, where \mathbf{s}_k^h is the h -frame state sequence², a_k is the applied action, o_t the observation, and s_{k+1} is the target next state. The corresponding h -frame target vertex positions are obtained by transforming mesh vertices with object pose sequence $\{\mathbf{x}_t \dots \mathbf{x}_{t-h+1}\}$, and collision information is calculated beforehand. The labels are the next frame's vertex positions, force, and torque readings. Random rotations sampled from the $SO(3)$ are applied to the training data as augmentation, and vertex positions are corrupted with Gaussian noise to increase training stability. All inputs/outputs are normalized during training.

b) *Loss function*: The loss is calculated as a weighted sum of three terms:

$$\mathcal{L} = \lambda_{\text{pos}} \mathcal{L}_{\text{pos}} + \lambda_f \mathcal{L}_f + \lambda_\tau \mathcal{L}_\tau \quad (8)$$

where \mathcal{L}_{pos} is the mean-squared-error of the predicted vertex positions and $\mathcal{L}_{f/\tau}$ are the MSE of the predicted F/T values. Based on empirical evaluation, we set $\lambda_{\text{pos}} = 1$, $\lambda_{f/\tau} = 0.1$.

IV. EXPERIMENT

With the thorough evaluations and baseline comparisons presented in [4], FIGNet has demonstrated its state-of-the-art performance in terms of contact resolution. Since the contact-conditional graph layers of our model are identical to FIGNet, the experiments here are focused on action/control related performance within the context of peg-in-hole task. We aim to show whether our model can provide an effective forward model for model-predictive control, and whether it can accurately approximate real-world dynamics. To evaluate its performance for control, we first train the model in MuJoCo simulation, and compare the success rates for peg

²In all following experiments $h = 3$ according to [4].

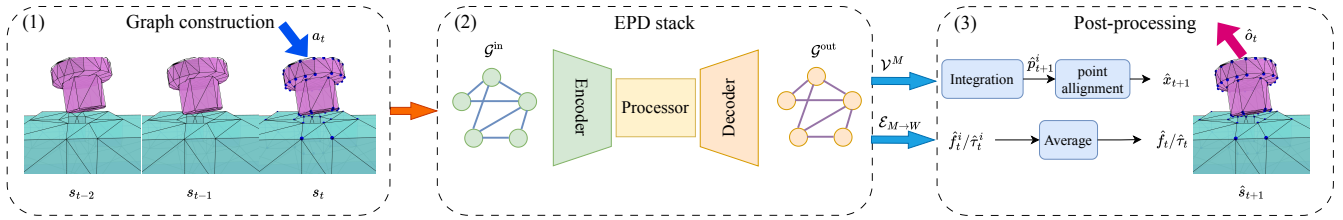


Fig. 1: Simulation pipeline overview. Cf. text for details about (1) Graph construction, (2)EPD stack, and (3) Post-processing.

insertion of an MPC agent using the trained model against one using ground truth dynamics model. In the real-world experiment, we train the model on data collected from our real-world setup and assess its accuracy in predicting end effector trajectories and F/T sensor readings. Finally, the learned model is deployed with a particle filter to track the robot’s end effector during real-world peg insertion.

A. Simulation experiment

a) *Data collection and training:* We build a MuJoCo simulation that mirrors our real-world setup: a UR10e robot with a primitive tool mounted on its end effector (see Fig. 3). During data collection, tool shapes are randomly chosen from three primitives (triangle, square, and hexagon). To diversify the training scene, three to six box obstacles of varying dimensions are placed and fixed on the table. The robot is driven by an impedance controller³, which accepts operational-space positional and rotational displacements as control targets; control signals are random splines generated at the start of each episode. Each episode comprises 400 control steps, each subdivided into 25 simulation sub-steps. We sample 500k steps for training and 25k for validation.

³Controller provided by robosuite [15].

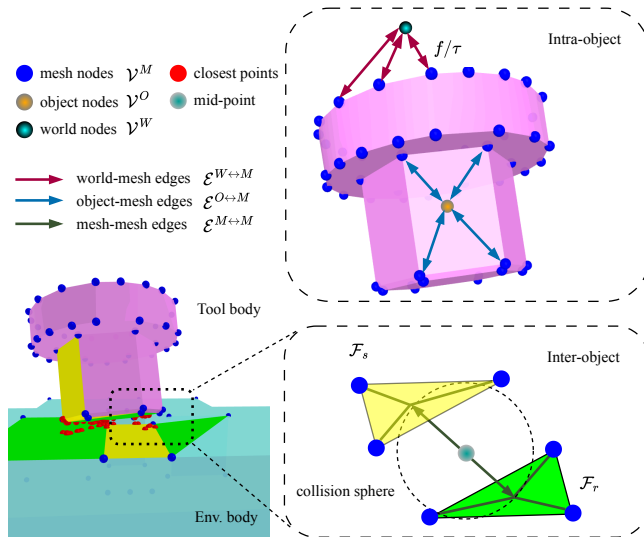


Fig. 2: Action-conditional edges between the world nodes and the tool mesh nodes (top). Face interaction mesh-mesh edges are created when two faces (\mathcal{F}_s and \mathcal{F}_r) fall within a predefined collision sphere (bottom).

The model is trained for 125k optimization steps with a batch size of 1028, and a decaying learning rate as in [4].

b) *Evaluation:* We evaluate the model’s effectiveness for model-based control on a peg insertion task. Since prediction accuracy is not the sole factor for successful control, we isolate the model’s performance from the influence of controller design by benchmarking it against the ground truth dynamics model, which is only accessible in simulation. Specifically, we use a sampling-based MPC agent, testing it first with the trained model, then with a baseline ground truth dynamics model provided by MJX⁴.

c) *Task description:* For the peg insertion task, we use the same UR10e robot and impedance controller as during data collection, mounting one of the 4 tool shapes on the robot’s end effector: triangle, square, hexagon, or circle. A matching slot with a nominal clearance of 5mm is fixed on the table (see Fig. 3). To evaluate the generalization to unseen geometries, the circle tool paired with a square slot is added, which were both excluded from the training set. The initial tool pose is randomly sampled near the slot. A trial is considered successful when the distance between the tool tip and slot bottom is less than 2 mm. The objective function for the trajectory optimization is defined as the exponential of the negative Euclidean distance (in meters) between the tool tip and the target position Δp_t ; and the exponential of the negative rotation difference $\Delta \theta_t$. A final reward of 10 is added when the distance falls below the threshold ϵ (2 mm):

$$r_t = 10 \cdot \mathbb{I}_{\|\Delta p_t\| \leq \epsilon} + \exp(-\|\Delta p_t\|) + \exp(-\|\Delta \theta_t\|) \quad (9)$$

For trajectory optimization, we employ the improved cross-entropy-method (iCEM) [17] for its efficiency with limited computational resources. Since the specifics of the MPC algorithm are not the focus of this work, agent parameters for both the learned and baseline models are empirically selected as listed in Table IV. We further examine the impact of domain-specific data by augmenting the training set with the data collected by the MPC agents described above. To this end, we introduce two additional models: the first, labeled as *Act-FIGNet-F*, is fine-tuned from the pre-trained model using only domain data, while the second (*Act-FIGNet-A*) is

⁴MJX is an official JAX-based re-implementation of the MuJoCo physics simulator, focusing on massive parallel simulation on acceleration hardware (GPU); although its simulation outcomes are not identical to the original MuJoCo, they closely match for the task considered in this work. We use MJX within the Brax library [16]; and also integrate our pipeline with the Brax API to enable seamless switch between MJX and Act-FIGNet.

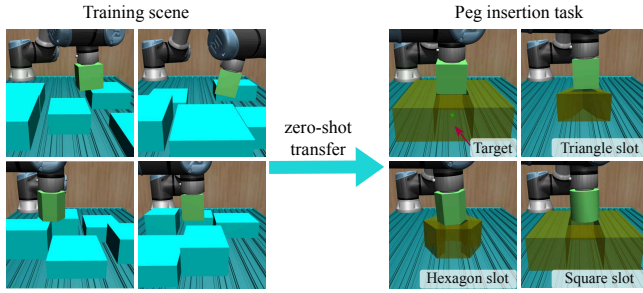


Fig. 3: The training scene consists of a UR10e robot with three random tool shapes and three to six box obstacles (left). Peg insertion task scene with different tools and their matching slot geometries (right).

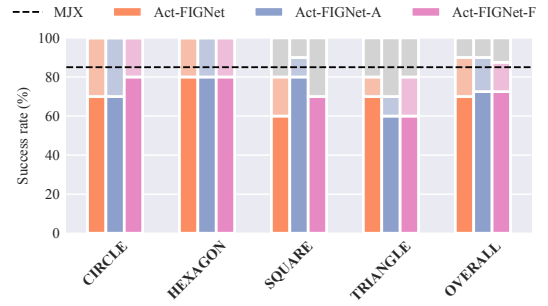
trained from scratch on the combined dataset. We evaluate each MPC agent over 40 task episodes (10 per tool shape), with each episode lasting up to 150 control steps.

d) Results: As shown in Fig. 4a, the MPC agent using the learned model achieves an overall success rate of 70%, and successfully inserts the peg halfway in 90% of all trials, which is comparable to the 85% success rate of the ground truth model. Notably, for the unseen circle tool shape, our model still attains a high success rate of 70%. The two additional models yield only marginal improvements, which suggests that our model does not rely heavily on domain-specific data. In summary, our trained model demonstrates a strong generalization ability to novel geometries, i.e., novel tool and slot shapes, and robustness to OOD actions.

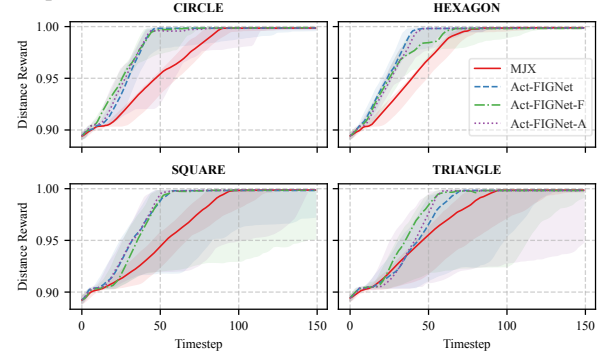
B. Real world experiment

a) Data collection and training: Real-world experiments are performed on a UR10e robot fitted with a high-precision force-torque sensor and a custom 3D-printed tool mounted on its end effector (Fig. 5). For this experiment, we collect data with two tool geometries, i.e., hexagonal and circular, against a complementary hexagonal slot with a nominal clearance of 1mm fixed on the test table (see Figure 5). The robot is controlled by Cartesian force controller [18] at 500Hz, whose control target changes at 10Hz and is randomly generated as in the simulation. To encourage contacts between the tool and the slot shape, the target force along the z -axis is randomly flipped to negative. At the start of each episode, the tool pose is reset randomly around the slot geometry. We record the control inputs as well as the end effector pose, velocity, and F/T readings. In total, 450k steps are sampled, of which 400k for training and 50k for testing. The model is trained for 120k steps with a batch size of 256. The data collection lasted for roughly 9h, while the training took around 24h on a NVIDIA RTX A6000 GPU.

b) Baselines: We select MuJoCo (MJX) as the baseline due to its high-fidelity contact dynamics. Previous work [4] also validated this choice, showing that MuJoCo outperforms PyBullet in the real-world dataset. However, the control interface in simulation differs from the real robot: the simulator uses joint torque control, whereas the physical robot



(a) Success rate comparison: solid bars are the actual success rates, and shaded bars indicate the percentage of episodes in which the peg was inserted at least halfway. The dashed line shows the average success rate with MJX over all tool shapes.



(b) Distance rewards comparison: shaded bands depict the confidence intervals, while solid lines indicate the median values.

Fig. 4: Results on the peg insertion tasks with different geometries. Performance comparisons of the MPC agent with the learned and baseline models are shown. The fine-tuned model is labeled as *Act-FIGNet-F*, while the model trained on the augmented dataset is labeled as *Act-FIGNet-A*.

operates under joint position/velocity control. To address this difference, we discard the robot structure completely and keep only the tool mounted on the end effector in simulation, where the tool is modeled as a rigid body with three hinge joints and a ball joint with an F/T sensor attached (see Fig. 5f). Control inputs are applied to the tool body directly as external forces. System parameters, including mass, diagonal inertia, joint damping, armature, and constraint solver parameters, are tuned to minimize the MSE between simulated and ground-truth trajectories and F/T readings over 20k steps of real-world data (see Appendix V-D for more details). As a second baseline, we evaluate an action-augmented version of FIGNet. This variant omits the action-conditional graph layers and instead concatenates control inputs directly to the vertex and object node features, with force-torque predictions decoded from object-vertex edge latents. To ensure a fair comparison, this baseline shares the same latent dimensions, MLP depth, and message-passing steps as our model, and is trained using the identical dataset and loss function.

c) Accuracy evaluation: To evaluate the accuracy of tool motion prediction, we calculate the 100-step (10s real-

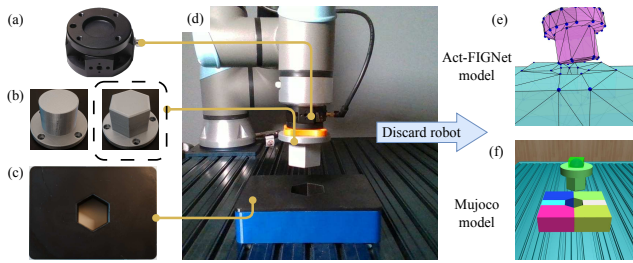


Fig. 5: (a) Bota SenseOne F/T sensor; (b) 3D printed tools; (c) Hexagonal slot with small clearance; (d) Setup for the real-world experiment with UR10e; (e) The system contains only the tool and world body represented with triangle meshes; (f) In MuJoCo, the tool is modeled as a floating free body with 3 hinge joints and a ball joint.

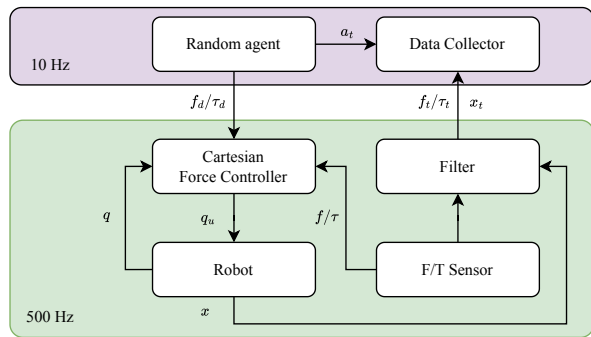


Fig. 6: Control and data collection pipeline for the real-world experiment. The random agent generates target wrench $\mathbf{f}_d/\boldsymbol{\tau}_d$ sent to the controller. The controller implements closed-loop force control, using the force-torque feedback $\mathbf{f}/\boldsymbol{\tau}$ and joint positions \mathbf{q} to calculate target joint positions \mathbf{q}_u sent to the robot. Tool pose \mathbf{x} is estimated from \mathbf{q} via forward kinematics. Since data collection and the control loop run at different frequencies, a filter is applied to synchronize and smooth the recorded data, i.e., F/T readings $\mathbf{f}_t/\boldsymbol{\tau}_t$ and tool pose \mathbf{x}_t .

world time) RMSE between predicted and ground-truth trajectories; and one-step errors for F/T precision evaluation. Since the absolute values of state changes are small, we also calculate the relative multi-step errors by dividing the absolute values with the accumulated state changes over the rollout. We sample 4k trajectories from the test set, each consisting of 100 consecutive steps, to compute the multi-step position and orientation RSME. Prediction sequences are generated by iteratively feeding the model’s output as the next input. One-step F/T prediction errors are calculated from 40k transitions. Table I summarizes the quantitative results. Our model achieves a 100-step RMSE of approximately 3.18 mm (16.04 %) in position and 0.866 deg (12.09 %) in orientation, both representing a more than 50 % reduction compared to MuJoCo. While less precise than our model, the simple action-augmented FIGNet (FIGNet+) still outperforms MuJoCo, consistent with the findings in [4]. Concurrently, our model achieves substantial lower F/T pre-

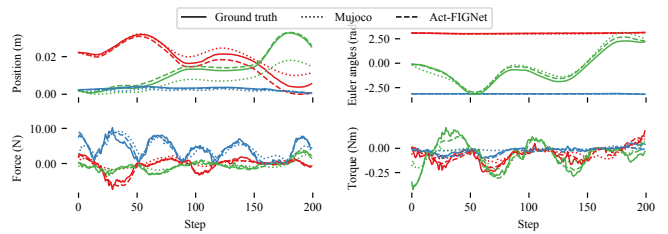


Fig. 7: An intuitive view of the prediction quality on real-world data compared with MuJoCo over 200 steps. Tool position and orientation (represented by Euler angles) are shown, with their values shifted for visualization (top). Force-torque predictions are also compared (bottom). The x, y, z components of all quantities are represented in red, green, and blue respectively.

diction errors than both baselines, with 0.663 N in force and 0.025 Nm in torque. This accuracy is also evident in Fig. 7, where predicted values closely follow the ground truth. The error comparison along the time step is illustrated in Fig. 9, while Fig. 7 and Fig. 11b provides qualitative examples of the tool pose and F/T predictions.

d) Action distribution shift: In practical peg insertion tasks, such as those involving standardized electrical connectors, object geometries and physical properties (e.g., friction) are typically known and exhibit limited variation. Therefore, the model’s robustness to out-of-distribution actions represents a more practical value. In the simulation experiments, we show that our model is robust to change in action distribution. To further validate this in real-world experiments, we evaluate the model on data collected with two additional control policies, i.e., a hand-coded peg insertion controller and a controller that moves the tools around the slot’s perimeter in circular paths, mimicking the hole searching motion. Details of these policies are described in Appendix V-E. The performed actions vastly differ from the training data (see Fig.17). With each policy, 20k steps of real-world interactions are sampled for evaluation. Figure 10, summarizes the results, showing only a slight increase in motion prediction errors under OOD actions. Notably, the motion errors are the highest during the expert peg insertion trajectories. This is expected, as small prediction errors in the xy -plane during peg insertion lead to large deviations in the z -axis. Despite this, one-step force-torque prediction remains accurate across both trajectory types. Fig. 8 illustrates a sample peg insertion trajectory, qualitatively demonstrating the model’s high prediction accuracy, including the ability to capture the discontinuities during contact (dis)engagement. While FIGNet+ achieves motion prediction accuracy comparable to our model, its F/T predictions are the least accurate. This suggests that the action-conditional graph layers in our model are particularly effective in capturing the relationship between control inputs and force-torque responses. The reduced torque error observed in the baselines may be attributed to the low magnitude of applied torque in these trajectories.

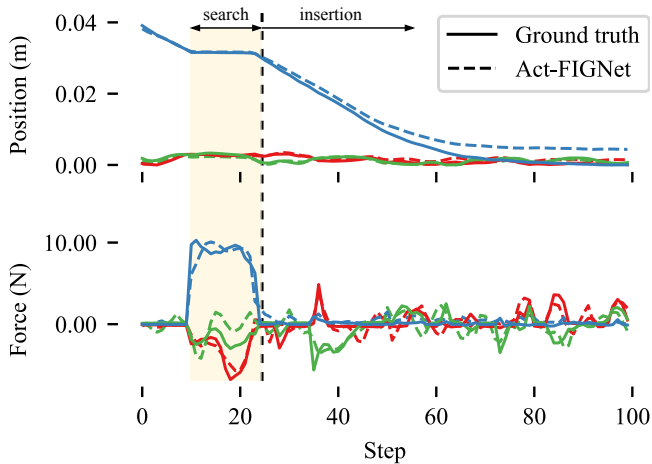


Fig. 8: Zero-shot transfer to actions sampled from an expert controller for the peg insertion task (same color scheme as Fig.7). The rendered rollout is shown in Fig. 11a.

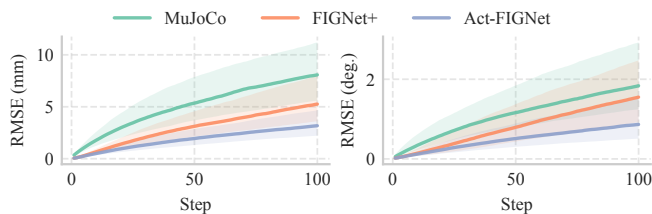


Fig. 9: Error comparison along the trajectories for position (left) and orientation (right). The plots display $RSME(T)$ for T ranging from 1 to 100.

C. State estimation with F/T readings

In the simulation experiments, we assumed perfect knowledge of the peg’s pose relative to the slot. In practice, this information needs to be estimated from sensors, such as camera, which is often corrupted by noise and subject to visual occlusion. Furthermore, as previously discussed, open-loop forward dynamics models suffer from accumulated errors, leading to significant drift over time. To address these, we can leverage the accurate one-step predictive models within a filtering framework to estimate the relative peg pose online, using F/T sensor data as observations.

In this experiment, we implement a simple particle filter

TABLE I: Prediction accuracy of Act-FIGNet, FIGNet variant (FIGNet+) and MuJoCo on real-world data. Shown are the 100-step RMSE for position and orientation; one-step F/T prediction error. Absolute (Abs.) and relative (Rel.) values are reported.

Model	$RSME^{pos}(T=100)$		$RSME^{rot}(T=100)$		One-step Error	
	Abs. (mm)	Rel. (%)	Abs. (deg)	Rel. (%)	Force (N)	Torque (Nm)
MuJoCo	8.08	41.23	1.837	29.45	2.349	0.086
FIGNet+	5.26	25.72	1.551	18.66	2.291	0.069
Ours	3.18	16.40	0.866	12.09	0.663	0.025

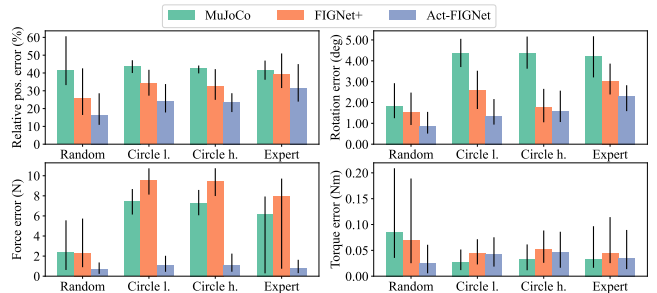


Fig. 10: Prediction errors under different policies. Expert policy performs peg insertion while the circle policy controls the tool to follow circular paths around the slot’s edge at two velocities (low and high). Absolute rotational error (degrees) is reported due to small overall orientation changes. Errors under the random policy are included for comparison.

that uses the learned dynamics model for motion updates, and the learned observation model for F/T measurement updates. The filter is configured with 30 particles and empirically selected noise parameters. To evaluate the contribution of each component, we tested three configurations. (1) **Motion-only**: open-loop prediction using only the learned dynamics model; (2) **particle filter with known pose**: a particle filter initialized with the ground truth pose. Estimates are corrected using F/T measurement updates following the motion updates.; (3) **particle filter with perturbation**: identical to (2) but the initial pose is corrupted with significant error, simulating an inaccurate initial estimate from a vision system.

The resulting estimation trajectories are illustrated in Fig. 12 to Fig. 14. A comparison between Fig. 12a and Fig. 12b reveals how the F/T observation model effectively corrects the motion model’s drift; this effectiveness persists even with noisy initial pose (Fig. 12c). As expected, the estimates rapidly converge to the ground truth upon making contact, especially along the z -axis, where the F/T observations are the most informative. More importantly, both the predicted (from the forward model) and estimated (from the filter) trajectories are physically plausible, with no interpenetration between objects, because the motion updates themselves are physically feasible. This is especially apparent along the z -axis, where the predicted and estimated values consistently remain above the ground truth. This demonstrates the potential of our learned models to complement visual data for state estimation in contact-rich manipulation tasks.

V. CONCLUSIONS

We presented an action-conditional learnable forward and observation model for peg-in-hole tasks. The model is trained via self-supervision and requires only robot joint encoder and force/torque readings for training, without privileged data and complicated calibration. The simulation experiment shows that our approach can be deployed in model-based control for peg insertion, even when neither the action distribution nor the environment geometries were encountered

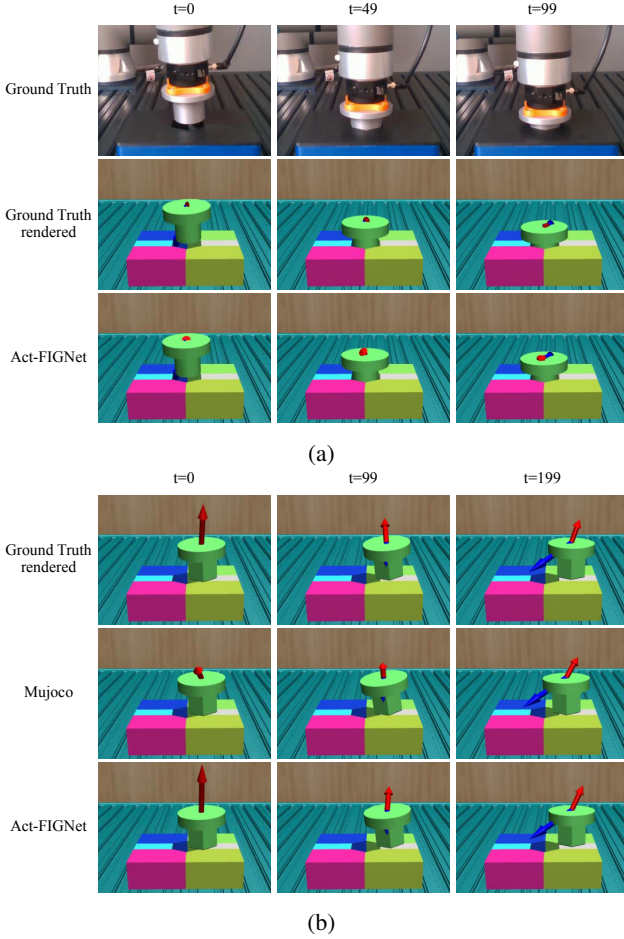


Fig. 11: Rendered prediction rollouts of real-world data. The blue arrows indicate control inputs, and the red arrows are the F/T readings. (a) Peg insertion trajectory shown in Fig. 8. (b) Test trajectory shown in Fig. 7. The robot is removed to render ground-truth data for visualization purposes.

during training; while the superior prediction accuracy on our real-world setup demonstrated the strength of a learnable dynamics model over analytical ones in capturing realistic contact dynamics. Furthermore, we showcased the potential of using the precise F/T observation model for state estimation in peg insertion tasks. However, our GNN model relies on specific functionalities of PyG [19], which are currently unavailable in its JAX equivalent (Jraph), resulting in a runtime approximately twice that of the purely JAX-based MJX. We attribute this overhead to implementation constraints, and anticipate that a future, unified JAX version would achieve runtime on par with the MJX. We believe that our work represents a significant step towards the practical application of learnable predictive models in real-world peg insertion tasks, and provides a meaningful foundation for future generalization to contact-rich manipulation. Future work will focus on improving our implementation and integrating uncertainty in the model for robust probabilistic state estimation.

A. Graph construction details

1) Node features:

a) *Mesh node*: Mesh node features are constructed by concatenating vertex velocities and the object’s static attributes. Vertex velocities are estimated by the difference between positions in two consecutive frames:

$$\mathbf{v}_i^{M,\text{feature}} = [\mathbf{p}_t^{m_i} - \mathbf{p}_{t-1}^{m_i}, \dots, \mathbf{p}_{t-h+1}^{m_i} - \mathbf{p}_{t-h}^{m_i}, \mathbf{k}] \quad (10)$$

where $\mathbf{p}_t^{m_i} \in \mathbb{R}^3$ is the vertex position, with the superscript, subscript $(\cdot)^{m_i}$, $(\cdot)_t$ indicating the vertex and time index respectively. Here, $\mathbf{k} = [m, \mu, b]$ represents the mass, friction coefficient and a binary variable related to its dynamic state. Object node features are computed similarly, but with object CoM instead of vertex positions. In real-world experiment, μ and m are kept the same for different tools, and $h = 3$ is used in all experiments, same as [4].

b) *World node*: There are two types of world nodes, i.e., type- f that apply forces, and type- τ that apply torques. Their features are simply one-hot vectors:

$$\mathbf{v}_f^{W,\text{feature}} = [0, 1, 0] \quad \mathbf{v}_\tau^{W,\text{feature}} = [0, 1, 0] \quad (11)$$

However, it is possibly beneficial to also add more information, such as the controller parameters.

2) Edge features:

a) *World-mesh edge*: In the direction from world to mesh nodes, the features are calculated as follows:

$$\mathbf{e}_{f \rightarrow m_i}^{\text{feature}} = [\mathbf{f}_t, \|\mathbf{f}_t\|] \quad (12)$$

$$\mathbf{e}_{\tau \rightarrow m_i}^{\text{feature}} = [\boldsymbol{\tau}_t, \|\boldsymbol{\tau}_t\|, \mathbf{p}_t^{m_i,o}, \|\mathbf{p}_t^{m_i,o}\|] \quad (13)$$

\mathbf{f}_t and $\boldsymbol{\tau}_t$ are the applied force and torque from the robot. $\mathbf{p}_t^{m_i,o}$ is the displacement between mesh vertex and body CoM. For the opposite direction, the edge features computed by adding negative signs to the corresponding vectors. Vector norms are concatenated following [4].

b) *Mesh-mesh edge*: In contrast to the face-face edges used in [4], we directly create edges between mesh nodes belonging to the potentially colliding faces. First, the collision detection algorithm⁵ provides the closest points on a colliding face pair, denoted as \mathbf{p}^s and \mathbf{p}^r . Next, the vertices of each face are ranked by their distances to the respective closest point, resulting in ordered vertex sets $\{\mathbf{p}^{m_{s_i}}\}_{i=1\dots 3}$ and $\{\mathbf{p}^{m_{r_i}}\}_{i=1\dots 3}$. In the following, we use m_s and m_r to denote the ordered vertex indices, i.e., $m_{s/r} = \{m_{s_i/r_i}\}_{i=1\dots 3}$. The edge features are then calculated the same as in [4]:

$$\mathbf{e}_{m_s \rightarrow m_r}^{\text{feature}} = [\mathbf{d}_{r_s}, [\mathbf{d}_{s_i}]_{i=1\dots 3}, [\mathbf{d}_{r_i}]_{i=1\dots 3}, \mathbf{n}_s, \mathbf{n}_r] \quad (14)$$

where $\mathbf{d}_{s_i/r_i} = \mathbf{p}_t^{m_{s_i/r_i}} - \mathbf{p}^{s/r}$ are the vectors from face vertices to their corresponding closest points; \mathbf{d}_{r_s} is the vector from \mathbf{p}_s to \mathbf{p}_r ; and \mathbf{n}_s and \mathbf{n}_r the normals of both faces. Message-passing for mesh-mesh connections is

⁵Implementation provided by the COAL library [20]

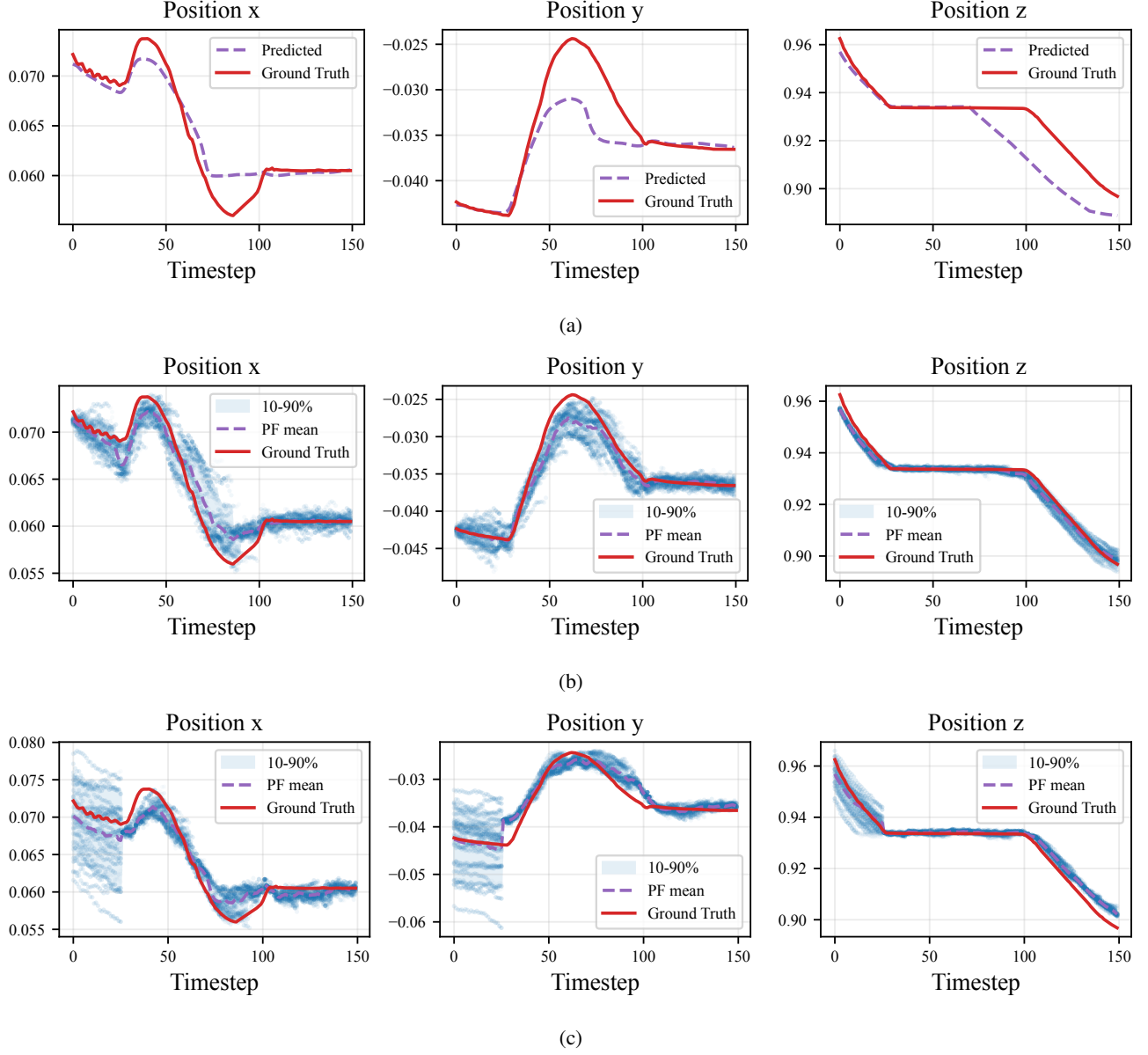


Fig. 12: Peg position estimation during a real-world peg insertion episode a using particle filter with F/T data. (a) open-loop prediction using dynamics model only. (b) Trajectory estimation using the particle filter with F/T correction, initialized at the ground-truth pose. (c) The same filter with F/T correction, but initialized with a random, inaccurate pose to simulate noisy perception.

handled differently: edge updates take into account all six sender and receiver nodes:

$$e_{m_s \rightarrow m_r}^{l+1} = \phi_{\mathcal{E}^M \rightarrow M}^{\text{proc}_l}([e_{m_s \rightarrow m_r}^l, \mathbf{v}_s^{M,l}, \mathbf{v}_r^{M,l}]) \quad (15)$$

$$\mathbf{v}_s^{M,l} = [\mathbf{v}_{s_i}^{M,l}]_{i=1\dots 3} \quad \mathbf{v}_r^{M,l} = [\mathbf{v}_{r_i}^{M,l}]_{i=1\dots 3} \quad (16)$$

First, the updated edge features are split into three vectors, one for each receiver node: $\{e_{m_s \rightarrow m_{r_i}}^{l+1}\}_{i=1\dots 3}$. Messages from face-face interaction are then aggregated for each mesh node m_j by summing up all incoming edge features:

$$\mathbf{h}^{m_j} = \sum_{\forall m_{r_i}=m_j} e_{m_s \rightarrow m_{r_i}}^{l+1} \quad (17)$$

Finally, the aggregated face-face messages are concatenated with the other aggregation to update the mesh node features, as shown in (4).

B. Model architecture details

The functions in the EPD stack, including encoders, decoders, node and edge functions are implemented as two-layer MLPs with ReLU activations. A LayerNorm module is applied after each MLP, except in the decoders. During message passing, inputs are added to the layer outputs to facilitate gradient flow. The implementation is built on PyTorch [21] and PyG [19]. See Table II for model parameters. The influence of message passing steps is evaluated on the

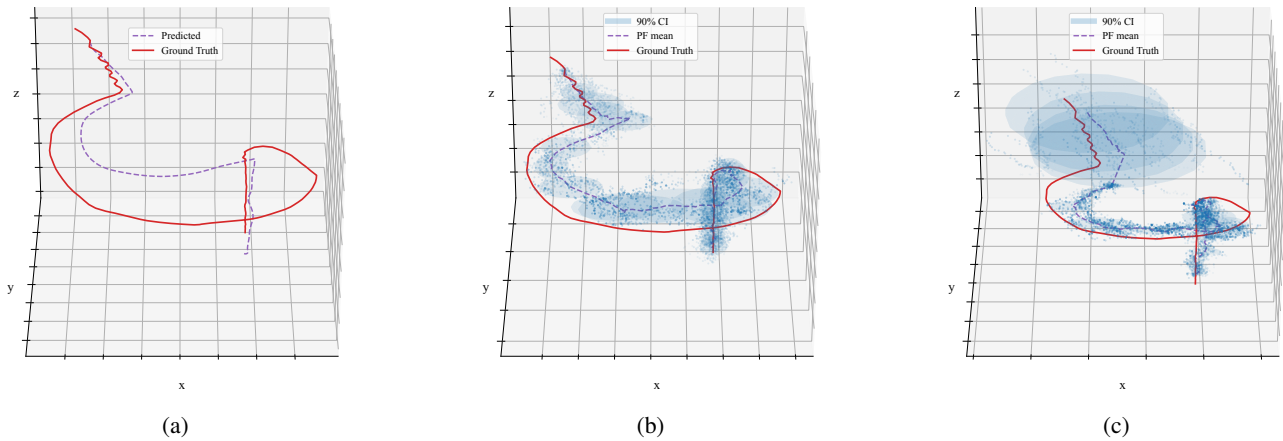


Fig. 13: 3D visualization of a sample peg insertion trajectory, complementing the 2D projection shown in Fig. 12. (a) Open-loop prediction. (b) Particle filter with accurate initialization. (c) Particle filter with noisy initial pose.

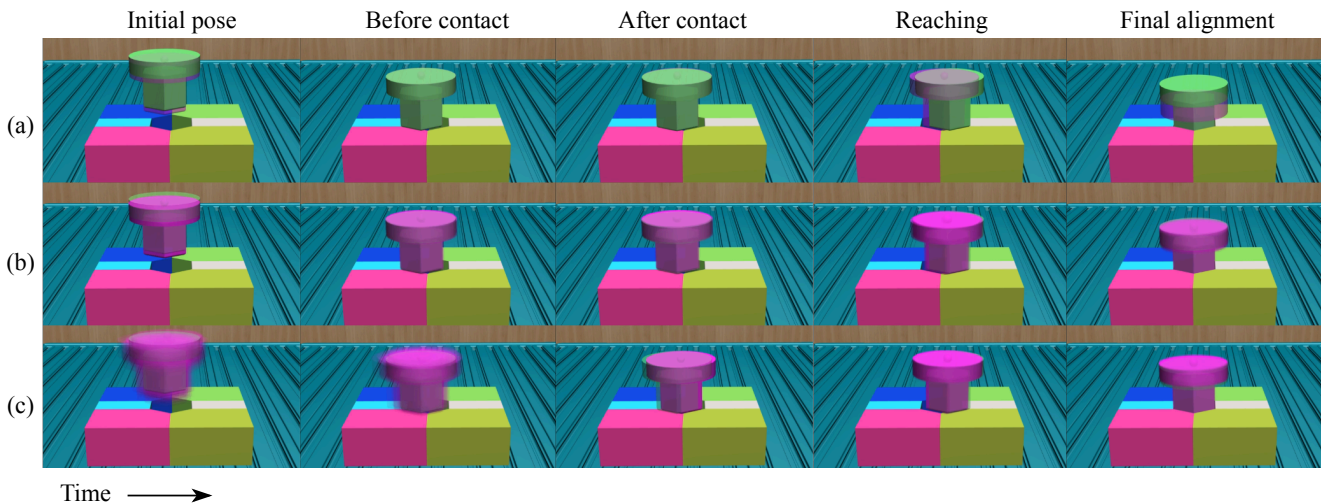


Fig. 14: Rendered images of the same real-world peg insertion episode shown in Fig. 12 and Fig. 13, overlaid with the particle filter estimates. The green tools represent ground truth, while the transparent magenta overlays represent the particle estimates/motion prediction. (a) Open-loop prediction. (b) Particle filter with accurate initialization. (c) Particle filter with noisy initial pose. The rendered video is included in the supplementary video. The magenta prediction in (a) is almost invisible before making contact because it closely follows the ground truth. In (b)-(c), due to the concentration of particles around the ground truth, the magenta overlays appear as a single solid body occluding the green ground truth.

real-world dataset, with results summarized in Table III. We observe that increasing the number of message-passing steps generally leads to improved prediction accuracy, with the best performance achieved at 10 steps. However, the improvement from 8 to 10 steps is relatively small. We also experimented with two different threshold values for collision detection, i.e., 1mm and 10mm, and found that its influence on the prediction accuracy is negligible, which we attribute to the low moving velocity in our datasets.

C. MPC agent details

Our MPC agent implementation is JAX-based and adapted from the MBRL-lib [22]. We use the iCEM as the optimizer, but since JAX does not support dynamic shapes, we fix the population size rather than using a decaying size as in

TABLE II: EPD stack parameters

Parameter	Value	Parameter	Value
Message passing steps	10	MLP hidden dimension	128
Edge feature dimension	128	MLP layers	2
Node feature dimension	128		

the original algorithm [17]. Since the dynamics models are employed deterministically, only one particle is used.

D. Baseline in real-world experiment

We tuned the parameters of the MuJoCo (MJX) baseline in two stages. First, we use 20 collision-free trajectories to adjust four parameters: mass, inertia, joint damping, and armature. A coarse grid search identifies the top five initial

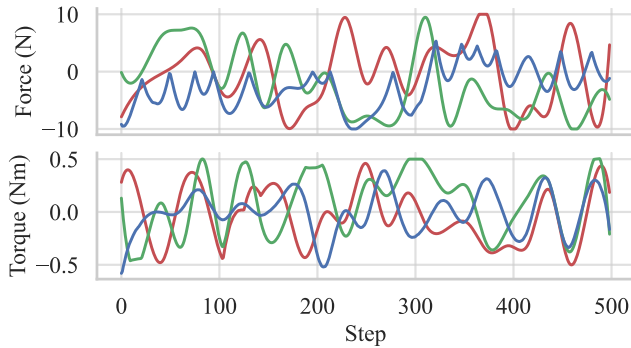
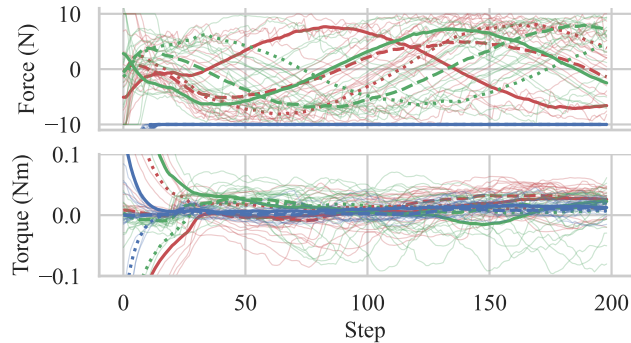
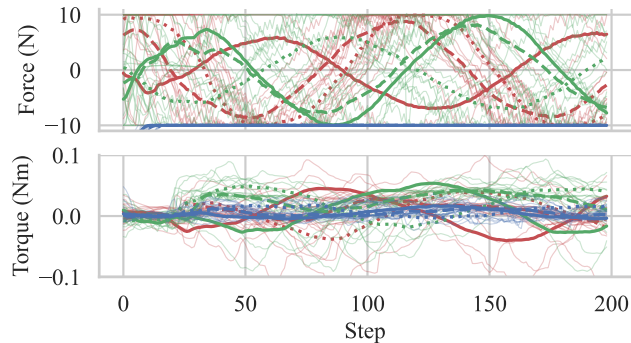


Fig. 15: A sample action sequence from the random policy used for training. The x , y , z components of the action values are shown in red, green and blue respectively.



(a) Circular trajectory policy with low velocity



(b) Circular trajectory policy with higher velocity

Fig. 16: Action sequences of circular trajectory policies. Sequences are grouped into tertiles for visualization, with the mean of each group plotted as solid, dashed, or dotted lines. A random subset of individual trajectories is shown in the background with low opacity.

TABLE III: Influence of message passing steps

Steps	RSME ^{pos} ($T=100$)		RSME ^{rot} ($T=100$)		One-step Error	
	Abs. (mm)	Rel. (%)	Abs. (rad)	Rel. (%)	Force (N)	Torque (Nm)
2	8.12	38.27	2.521	30.53	0.909	0.036
4	3.60	19.20	3.058	38.12	0.741	0.028
6	3.56	19.08	1.189	16.10	0.766	0.028
8	3.23	17.79	1.097	15.20	0.727	0.024
10	3.18	16.40	0.866	12.09	0.663	0.025

TABLE IV: MPC Agent Parameters

Parameter	Value	Description
Particles	1	Number of particles
Horizon	50	Planning horizon
Samples	20	Population size for CEM solutions
Iterations	5	Optimization iterations
Replan freq.	5	Frames to execute before replanning

guesses, which are then refined using the BFGS algorithm to minimize the MSE between simulated and ground truth trajectories. Second, we use another 20 trajectories involving collisions to further fine-tune these parameters, along with four additional constraint solver parameters (`solref`, `solimp`), optimizing for both trajectory and F/T errors.

E. Control policies

a) Random policy for training: We adopt the random trajectory generation method described in [5]. First, random points are sampled uniformly within action limits, where the number of points corresponds to the episode length. An action sequence is then generated via cubic spline interpolation between these points. A representative action sequence is shown in Fig. 15. Safe execution is ensured by a bounded workspace for the end effector. Exceeding these limits triggers a virtual spring force that pulls the end effector back into the valid workspace.

b) Peg insertion policy: The tool initially descends to establish surface contact, after which the controller executes a spiral search trajectory in the xy -plane centered at the target (the bottom of the slot). The spiral motion is coupled with a constant downward force to ensure surface contact.

c) Circular trajectory policy: The tool first moves down to establish contact with the surface, then follows circular paths around the hole’s perimeter. We test with two different velocities to evaluate the model’s robustness to action frequency change. In low velocity, the tool completes one full circle in 200 steps (20s), while in high velocity, it completes three circles in the same number of steps. The high-velocity policy generates similar action frequencies as the training data, while the low-velocity one is slower.

Fig. 17 illustrates the action distributions of different policies. The distributions shift significantly from the random actions used for training to the ones from additional policies used for testing.

ACKNOWLEDGMENT

The DFKI Niedersachsen is sponsored by the Ministry of Science and Culture of Lower Saxony and the VolkswagenStiftung. This work was funded through a grant of the German Federal Ministry for Economic Affairs and Climate Action with the grant number 01ME19003D. We thank Yulia Rubanova for her valuable advice on the model implementation.

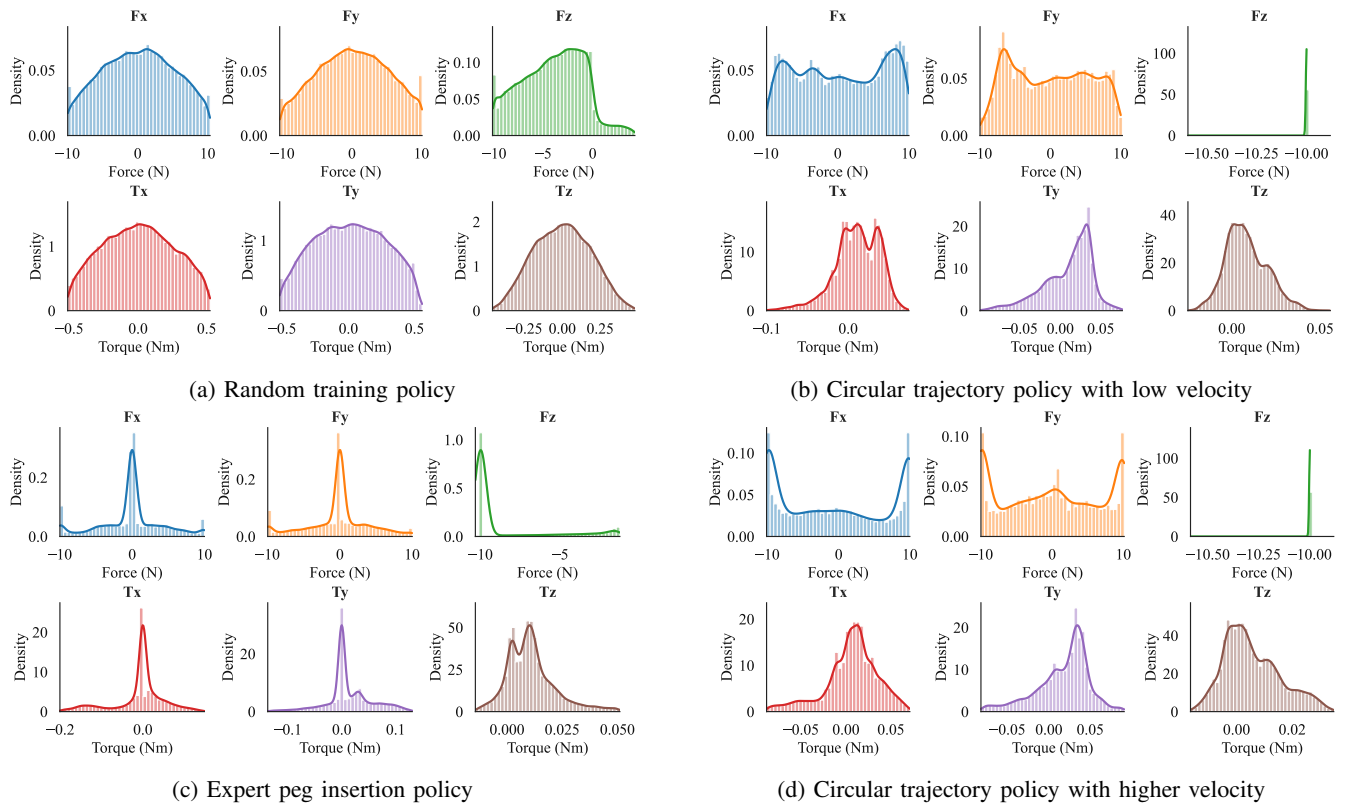


Fig. 17: Action distributions of different control policies.

REFERENCES

- [1] E. Todorov, T. Erez, and Y. Tassa, “Mujoco: A physics engine for model-based control,” in *IROIS*. IEEE, 2012, pp. 5026–5033.
- [2] E. Coumans and Y. Bai, “Pybullet, a python module for physics simulation for games, robotics and machine learning,” <http://pybullet.org>, 2016–2021.
- [3] K. R. Allen, T. Lopez-Guevara, *et al.*, “Graph network simulators can learn discontinuous, rigid contact dynamics,” in *CoRL*, ser. Proceedings of Machine Learning Research, vol. 205. PMLR, 2022, pp. 1157–1167.
- [4] K. R. Allen, Y. Rubanova, *et al.*, “Learning rigid dynamics with face interaction graph networks,” in *ICLR*. OpenReview.net, 2023.
- [5] A. Sanchez-Gonzalez, N. Heess, *et al.*, “Graph networks as learnable physics engines for inference and control,” in *ICML*, ser. Proceedings of Machine Learning Research, vol. 80. PMLR, 2018, pp. 4467–4476.
- [6] Y. Li, J. Wu, *et al.*, “Propagation networks for model-based control under partial observation,” in *ICRA*. IEEE, 2019, pp. 1205–1211.
- [7] T. Pfaff, M. Fortunato, A. Sanchez-Gonzalez, and P. W. Battaglia, “Learning mesh-based simulation with graph networks,” in *ICLR*. OpenReview.net, 2021.
- [8] A. Wei and O. Fink, “Integrating physics and topology in neural networks for learning rigid body dynamics,” *Nature Communications*, vol. 16, no. 1, p. 6867, 2025.
- [9] J. Pankert and M. Hutter, “Learning contact-based state estimation for assembly tasks,” in *IROIS*, 2023, pp. 5087–5094.
- [10] A. Negi, O. M. Manyar, D. K. V. Pennetsa, and S. K. Gupta, “Learning the contact manifold for accurate pose estimation during peg-in-hole insertion of complex geometries,” *CoRR*, vol. abs/2505.19215, 2025.
- [11] K. Gadeyne, T. Lefebvre, and H. Bruyninckx, “Bayesian hybrid model-state estimation applied to simultaneous contact formation recognition and geometrical parameter estimation,” *Int. J. Robotics Res.*, vol. 24, no. 8, pp. 615–630, 2005.
- [12] J. Kim, Y. Zhu, and A. M. Dollar, “Tactile probabilistic contact dynamics estimation of unknown objects,” *CoRR*, vol. abs/2409.17470, 2024.
- [13] K. Tracy, Z. Manchester, *et al.*, “Efficient online learning of contact force models for connector insertion,” *CoRR*, vol. abs/2312.09190, 2023.
- [14] N. Ravi, J. Reizenstein, *et al.*, “Accelerating 3d deep learning with pytorch3d,” *CoRR*, vol. abs/2007.08501, 2020.
- [15] Y. Zhu, J. Wong, A. Mandlekar, and R. Martín-Martín, “robosuite: A modular simulation framework and benchmark for robot learning,” *CoRR*, vol. abs/2009.12293, 2020.
- [16] C. D. Freeman, E. Frey, *et al.*, “Brax - A differentiable physics engine for large scale rigid body simulation,” *CoRR*, vol. abs/2106.13281, 2021.
- [17] C. Pinneri, S. Sawant, *et al.*, “Sample-efficient cross-entropy method for real-time planning,” *CoRR*, vol. abs/2008.06389, 2020.
- [18] S. Scherzinger, A. Roennau, and R. Dillmann, “Forward dynamics compliance control (FDCC): A new approach to cartesian compliance for robotic manipulators,” in *IROIS*. IEEE, 2017, pp. 4568–4575.
- [19] M. Fey, J. Sunil, *et al.*, “Pyg 2.0: Scalable learning on real world graphs,” *CoRR*, vol. abs/2507.16991, 2025.
- [20] J. Pan, S. Chitta, *et al.*, “Coal: an extension of the flexible collision library,” <https://github.com/coal-library/coal>, 2015–2024.
- [21] J. Ansel, E. Z. Yang, *et al.*, “Pytorch 2: Faster machine learning through dynamic python bytecode transformation and graph compilation,” in *ASPLOS (2)*. ACM, 2024, pp. 929–947.
- [22] L. Pineda, B. Amos, *et al.*, “Mbrl-lib: A modular library for model-based reinforcement learning,” *CoRR*, vol. abs/2104.10159, 2021.